Magnetic ordering and charge transport in electron-doped La$_{1-y}$Ce$_y$MnO$_3$ (0.1 ≤ y ≤ 0.3) films

V.G. Prokhorov, G.G. Kaminsky, and V.S. Flis

Institute for Metal Physics, National Academy of Sciences of Ukraine, Kiev 03142, Ukraine
E-mail: pvg@imp.kiev.ua

Y.H. Hyun, S.Y. Park, and Y.P. Lee

q-Psi and Department of Physics, Hanyang University, Seoul 133-791, Korea

V.L. Svetchnikov

National Center for HREM, TU Delft 2628AL, The Netherlands

Microstructure, magnetic and transport properties of the as-deposited La$_{1-y}$Ce$_y$MnO$_3$ (0.1 ≤ y ≤ 0.3) films, prepared by a pulse laser deposition, have been investigated in wide region of temperature and magnetic field. The microstructure analysis reveals that all films have a high c-oriented texture, the orthorhombic crystal lattice and the negligible quantity of CeO$_2$ inclusions. The observed strip-domain phase with a periodic spacing of about $3c$, the crystal lattice of which is the same to the basic film phase, reveals the magnetic behavior typical for the Griffiths phase. The regions of the double-period modulated phase was found at room temperature in the $y = 0.1$ film, which are treated as the Mn^{3+}/Mn^{2+} ordering with the partial ferromagnetic → antiferromagnetic transition at T_N ≤ 80 K. At the same time, the carried out investigation manifests that the magnetic and transport properties of the electron-doped La$_{1-y}$Ce$_y$MnO$_3$ films, driven by a cation doping, are similar to that for the hole-doped La/Ca manganites. Therefore, one can conclude, that does not exist of a principle difference between the mechanisms of spin-ordering and charge-transport in the hole- and the electron-doped manganites.

1. Introduction

The hole-doped manganites L$_{1-x}$A$_x$MnO$_3$, where L and A are a trivalent lanthanide ion and a divalent alkaline-earth ion, respectively, have attracted considerable attention due to their interesting fundamental science, connected with the discovery of colossal magnetoresistance (CMR), and potential for applications [1]. The transport and magnetic properties of doped manganites are interpreted as a rule within the framework of «double exchange» (DE) model which considers the magnetic coupling between Mn^{3+} and Mn^{4+} that results from the motion of an itinerant electron between two partially filled d shells with strong on-site Hund's coupling [2–4]. However, Millis et al. [5] have shown that DE mechanism alone cannot explain all aspects of CMR effect, particularly the temperature dependence of resistance, $R(T)$, above the metal–insulator (MI) transition temperature. The authors suggest that a polaron effect due to a strong electron–phonon coupling arising from the Jahn–Teller distortion of the Mn^{3+} ions is a necessary component for explaining the details of the $R(T)$ behavior above the Curie point (T_C). Taking into account, that while Mn^{3+} is a Jahn–Teller ion, Mn^{4+} and Mn^{2+} are both non-Jahn–Teller ions, one can expect that the substitution of a triva-

lent lanthanide by a tetravalent element, instead of a divalent one, leads to the same result due to an origin of the DE between Mn^{3+} and Mn^{2+}. $La_{1-y}Ce_yMnO_3$ is a typical electron-doped system which demonstrates the MI transition and the ferromagnetism (FM) similar to that for the hole-doped manganites [6]. However, numerical publications reveal that the single-phase $La_{1-y}Ce_yMnO_3$ compound can be prepared only by the laser-pulse-deposition method at certain technological conditions [7–13]. At the same time, the collected data on the hole-doped manganites testify that the magnetic and the electronic phase diagrams of thin films are significantly different from that for the bulk and, therefore, it is desirable to perform an additional experimental study.

In this paper we report the experimental results for the as-deposited $La_{1-y}Ce_yMnO_3$ ($0.1 \leq y \leq 0.3$) films, prepared by the laser ablation. It was shown that the magnetic and the transport properties of the investigated films, driven by a cation doping, are very similar to that for the hole-doped $La_{1-y}Ca_yMnO_3$ system. The observed evidence for the charge-ordered antiferromagnetic (AFM) state and the Griffiths phase is explained by the microstructure features of the films.

2. Experimental techniques

A cross-beam laser-ablation technique was employed for the preparation of the films. A detailed description of the technique was presented elsewhere [14]. We used two Nd-YAG lasers with a wavelength of 1064 nm, a pulse duration of 7.8–10.5 ns, a pulse-repetition rate of 20 Hz, and an energy of 0.3 J/pulse. The power density of laser beam focused on the target was $9.5 \cdot 10^8$–$2 \cdot 10^{10}$ W/cm^2. The targets were manufactured from the powders of the stoichiometric composition by hot-pressing and heating at 1200 °C for 4 days in air. The oxygen pressure in chamber was 200 Torr during deposition and 600 Torr during cooling. Under these conditions were grown the $La_{0.9}Ce_{0.1}MnO_3$ (LCMO9), the $La_{0.8}Ce_{0.2}MnO_3$ (LCMO8), and the $La_{0.7}Ce_{0.3}MnO_3$ (LCMO7) films with the same thickness of $d \simeq 300$ nm. The substrate was a $LaAlO_3$ (100) single crystal (LAO) with an out-of-plane lattice parameter $c \simeq 0.379$ nm for the pseudocubic symmetry. The substrate temperature during deposition was 770 °C, and only the as-deposited films were used for study. The θ–2θ x-ray diffraction (XRD) patterns were obtained using a Rigaku diffractometer with Cu K_α radiation. The lattice parameters evaluated directly from the XRD data were plotted against $\cos^2\theta/\sin\theta$. From the intercept of the extrapolated straight line to $\cos^2\theta/\sin\theta = 0$, a more precise lattice parameter was obtained. The high-resolution electron-microscopy (HREM) and electron-diffraction studies were carried out using a Philips CM300UT-FEG microscope with a field emission gun operated at 300 kV. The point resolution of the micro-

scope was in the order of 0.12 nm. The cross-sectional specimens were prepared by the standard techniques using mechanical polishing followed by ion-beam milling at a grazing incidence. All microstructure measurements were carried out at room temperature. The magnetic measurements were performed by using a Quantum Design SQUID magnetometer. The resistance measurements were performed by using the four-probe method in a temperature range of 4.2–300 K and in a magnetic field up to 5 T.

3. Microstructure

Figure 1 presents the θ–2θ XRD scans for LCMO9 (*a*), LCMO8 (*b*) and LCMO7 (*c*) films, which display the well-defined (00*l*) Bragg peaks of high intensity for the films (F) and the LAO substrate (S), indicating that the deposition results in a highly *c*-oriented crystal structure. At the same time, the additional peaks near the 2θ angles of 33 and 70° are existent, manifesting the presence of a second phase. Commonly this phase identify as the unreacted cerium dioxide (CeO_2) impurity, which is more
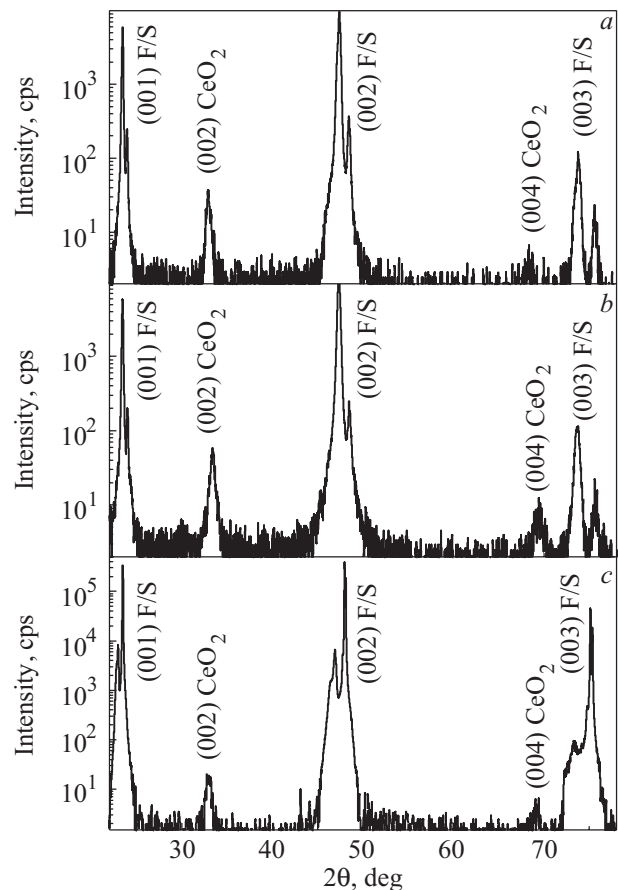

Fig. 1. θ–2θ XRD scans for the $La_{1-y}Ce_yMnO_3$ films with $y = 0.1$ (*a*), 0.2 (*b*) and 0.3 (*c*). F and S denote the film and the substrate, respectively. The Bragg peaks are identified for a simple pseudocubic symmetry.

stable relative to the basic La$_{1-y}$Ce$_y$MnO$_3$ compound. It is confirmed by the calculated lattice parameter of the impurity phase from θ–2θ XRD scans, $a \simeq 0.543$ nm, which is excellently coincident with the published results for CeO$_2$ [15,16]. Analysis of the XRD data for La$_{1-y}$Ce$_y$MnO$_3$ reveals that the out-of-plane lattice parameter (c) for pseudocubic symmetry slightly decreases with the Ce doping following to the empirical expression: $c = c_0 - 0.005y$, where $c_0 = 0.3885$ nm. The found tendency for c completely agrees with the data, which were obtained for the La$_{1-y}$Ce$_y$MnO$_3$ films early [11,12], and is typical for the hole-doped manganites, such as La$_{1-y}$Ca$_y$MnO$_3$ [17].

Figure 2,*a* exhibits the low-magnification cross-sectional HREM images of the LCMO9 film, manifesting that the column-like microstructure is formed during the deposition with the well-defined sharp and flat interface between film and substrate. The average diameter of a column turns out to be about 20 nm (see inset in Fig. 2,*a*). The carried out HREM study of the LCMO8 and LCMO7 films (not shown) reveals the same column-like microstructure. The similar morphological feature of microstructure has been already observed in the La$_{1-y}$Ca$_y$MnO$_3$ films [18–20], and is explained by a dislocation-free epitaxial growth mode with the formation of a strong lattice-strained state. These biaxial strains accommodate, during the film growth, in forming a coherent columnar microstructure directed along interface normal which can be treated as prismatic antiphase boundaries.

The high-magnification cross-sectional HREM image of LCMO9, represented by Fig. 2,*b*, shows that the major part of the film has a perfect crystal lattice. This is confirmed by the corresponding fast Fourier transform (FFT) for this image (see Fig. 2,*c*), which reveals the almost rectangular pattern only of basic Bragg spots, typical for close to the orthorhombic crystal structure. At the same time, the more careful analysis of a few HREM images shows that the angle between ortogonal atomic rows is near 89.2°, indicating the slight rhombohedral crystal lattice distortion of the LCMO9 film. In contrast to that the high-magnification HREM images and the FFT patterns for the LCMO8 and LCMO7 films (not shown) manifest only the right angle between atomic rows, indicating the formation of the undistorted orthorhombic crystal lattice. The analysis of interspot spacings on the FFT patterns and the HREM images reveals that these films have the following lattice parameters (for pseudocubic symmetry): $c \simeq 0.3887$, 0.3877 and 0.3867 nm, and $a \simeq b \simeq 0.3814$, 0.382 and 0.3823 nm for LCMO9, LCMO8 and LCMO7, respectively. It is clear that the cross-sectional HREM analysis can not distinguish difference between a and b in-plane parameters. In spite of that the obtained lattice parameters are good coincident with the XRD data.
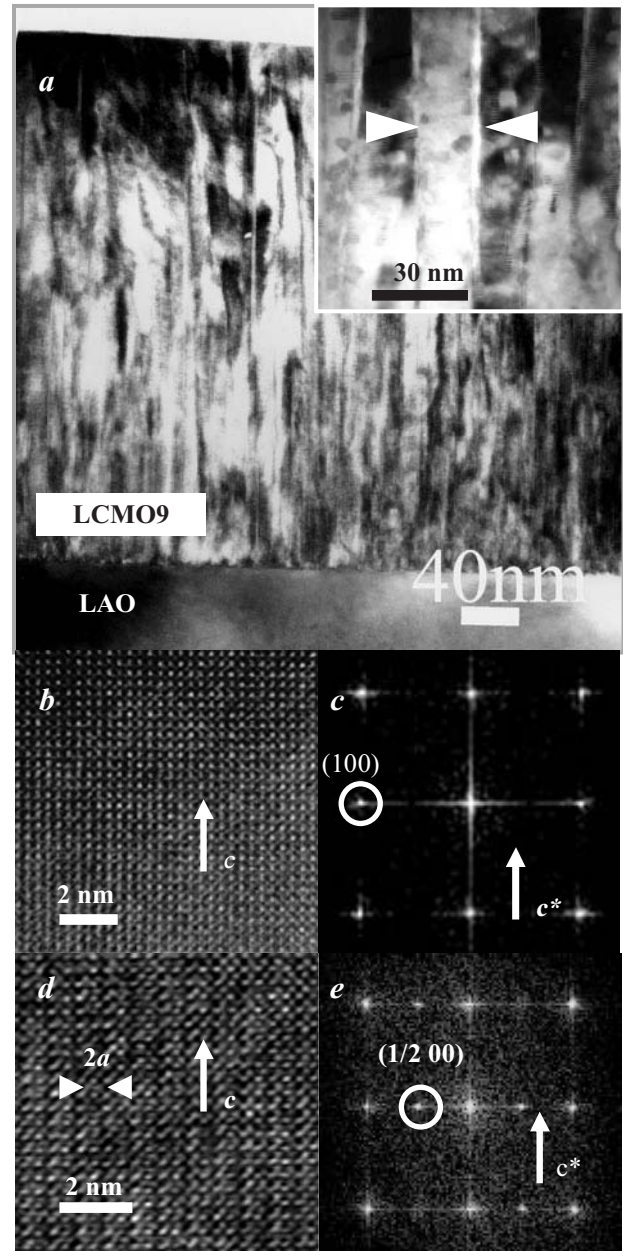

Fig. 2. (*a*) Low-magnification cross-sectional HREM image for the La$_{0.9}$Ce$_{0.1}$MnO$_3$ film. LAO denotes a substrate. Inset presents the column-like microstructure with an average diameter of a column about 20 nm (indicated by arrows). [(*b*) and (*c*)] The high-magnification cross-sectional image and the corresponding FFT pattern for major part of this film. Only the fundamental Bragg peaks are indicated. [(*d*) and (*e*)] The same pictures for the modulated phase with the doubled *a*-axis lattice period parallel to the *c*-axis direction. The presence of superlattice spots with a modulation wave vector, similar to 1/2, 0, and 0, is evident.

The main microstructural peculiarity of the LCMO9 film, which is not observed in the LCMO8 and LCMO7 ones (in addition to the rhombohedral distortion), is presence of the small regions of double-period modulated

phase, represented by Fig. 2,*d*. In this case the FFT of HREM image (see Fig. 2,*e*) produces not only a rectangular pattern of the fundamental Bragg spots, which are typical for a regular pseudocubic crystal lattice, but additional superlattice reflections with a wave vector $q = a^*/2$ (indicated by a white circle), where a^* is the *a*-axis reciprocal lattice vector. The similar superlattice spots in FFT pattern have already been observed for the hole-doped La$_{1-y}$Ca$_y$MnO$_3$ films, including composition of $y = 0.1$, and treated as appearance of a charge ordering of the Mn^{4+} and the Mn^{3+} ions [21–23]. Like the hole-doped manganites, there is no sharp boundary between modulated and unmodulated regions. Instead, one phase is blended gradually with the other.

The another crystal-lattice imperfections, which are typical for the all made films, are connected with the presence of the CeO$_2$ and, so-called, the strip-domain phases. Figures 3,*a* and *b* display the cross-sectional high-magnification HREM image and the corresponding FFT pattern, respectively, for the LCMO9 film in the area of the coexisting the LCMO9 and the CeO$_2$ crystalline phases. It is seen that, in contrast to the modulated and unmodulated regions, the interphase boundary (indicated by dashed line) is the very sharp. The orientation relationship between these phases is [110]$_{CeO_2}$ || [001]$_{LCMO9}$, giving evidence that the crystal lattice of the CeO$_2$ inclusion is rotated on angle of 45° against to the matrix LCMO9 phase. The CeO$_2$ phase does not exceed a few percent of the film volume and has an average size of 100 nm. Figures 3,*c* and *b* present the HREM image and the FFT pattern for the strip-domain phase, respectively. The similar long-periodic modulation of crystal structure has already been observed in the electron- and the hole-doped manganites, and was identified as the nanoclustering CeO$_2$ domains [13,24] or attributed to a specific ordering of the La and the doped ions [22,25]. The FFT of the HREM image for the strip-domain phase (see Fig. 3,*d*) manifests a rectangular pattern of the fundamental Bragg spots, typical for the matrix LCMO9 phase, and the additional superlattice reflections (indicated by white arrows), corresponding to the strip-domain modulation. Therefore, the strip-domain phase has a crystal structure similar to main
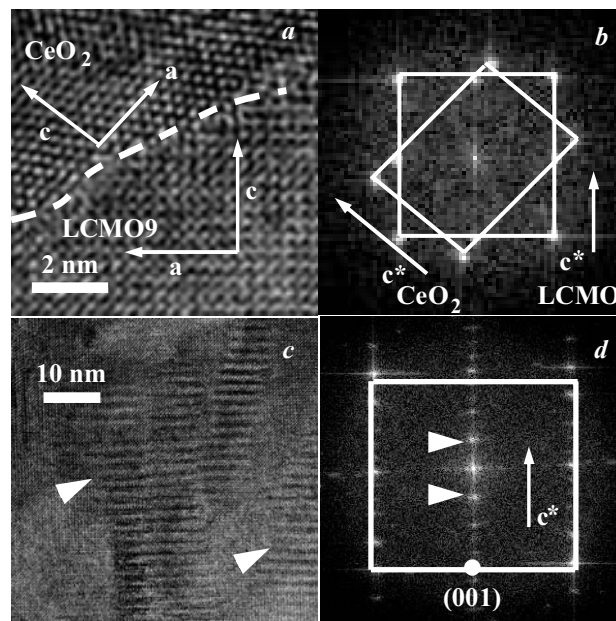

Fig. 3. [(*a*) and (*b*)] The high-magnification cross-sectional image and the corresponding FFT pattern for the La$_{0.9}$Ce$_{0.1}$MnO$_3$ film area where the basic and the CeO$_2$ phases coexist. The dashed line indicate the interphase boundary. [(*c*) and (*d*)] The same pictures for the strip-domain phase. The white arrows indicate the period of strip domains in the (*c*) real and the (*d*) reciprocal space. The white square in the (*d*) evidences that the strip-domain phase has a crystal lattice of the basic phase.

phase of the film, and cannot to identify as the nano-clustering CeO$_2$ domains. More preferable seems to be explanation based on the Wigner-crystal model (or similar to that), which takes into account the distribution of the doped ions in the La-based manganites [25–29]. It is found that La/Ca ordering along with Mn^{3+} and Mn^{4+} stripes in La$_{1-y}$Ca$_y$MnO$_3$ is more energetically favorable than La/Ca disordering that can lead to formation of the strip-domain structure, whose domain period, D_{SD}, is equal to an integer of the crystal lattice parameters. The FFT pattern in Fig. 3,*d* reveals that $D_{SD} \simeq 3c$ in our case.

The data of the XRD and the HREM study are summarized in the Table 1.

Table 1. Results of the XRD and the HREM analysis for the investigated films

Samples	Crystal structure	Out-of-plane lattice parameter c, nm[a]		Tetragonal ratio c/a	Lattice parameter of CeO$_2$ inclusion, a, nm	XRD intensity ratio at (002) Bragg peak
		XRD	HREM data	HREM data	XRD data	I_{CeO}/I_{Film}, %
LCMO9	Rhombohedral	0.388	0.3887	1.02	0.543	0.9
LCMO8	Orthorombic	0.3875	0.3877	1.015	0.544	0.08
LCMO7	Orthorombic	0.387	0.3867	1.012	0.543	0.07

[a] For pseudocubic symmetry.

4. Experimental results

Figure 4 shows the in-plane field-cooled (FC) (solid symbols) and the zero-field-cooled (ZFC) (open symbols) temperature dependences of the magnetic moment, $M(T)$, for the LCMO9 (*a*), LCMO8 (*b*) and LCMO7 (*c*) films at different applied magnetic fields. All films manifest the ferromagnetic transition at the Curie temperature $T_C \simeq 150$, 250 and 280 K, for LCMO9, LCMO8 and LCMO7, respectively. The obtained results are very close to the published data for the bulk and the as-deposited films [9–13,24]. The observed splitting between ZFC and FC $M(T)$ curves in a low-temperature range at $H = 0.01$ T can be explained by the existent difference between an applied magnetic field direction and the easy magnetization axis. Assuming that, in spite of the high *c*-oriented
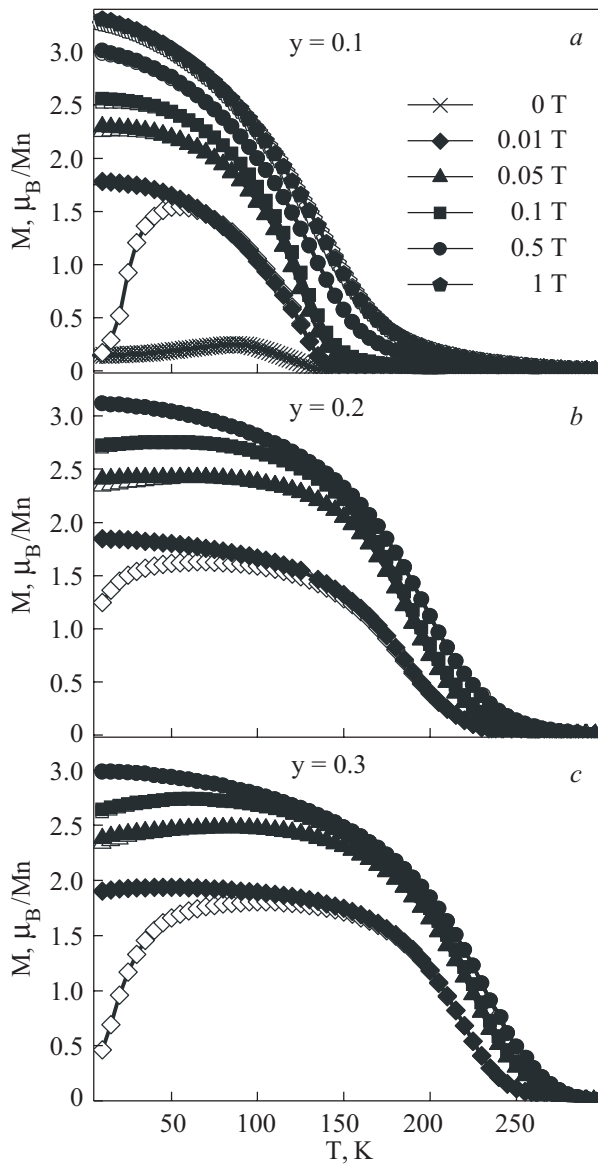
texture, the column-like crystallites have a slight disorientation to each other in the *ab* plane, one can conclude that the easy magnetization axes are randomly oriented, as well. Therefore, the difference between ZFC and FC $M(T)$ curves can be treated as a characteristic of the mi-
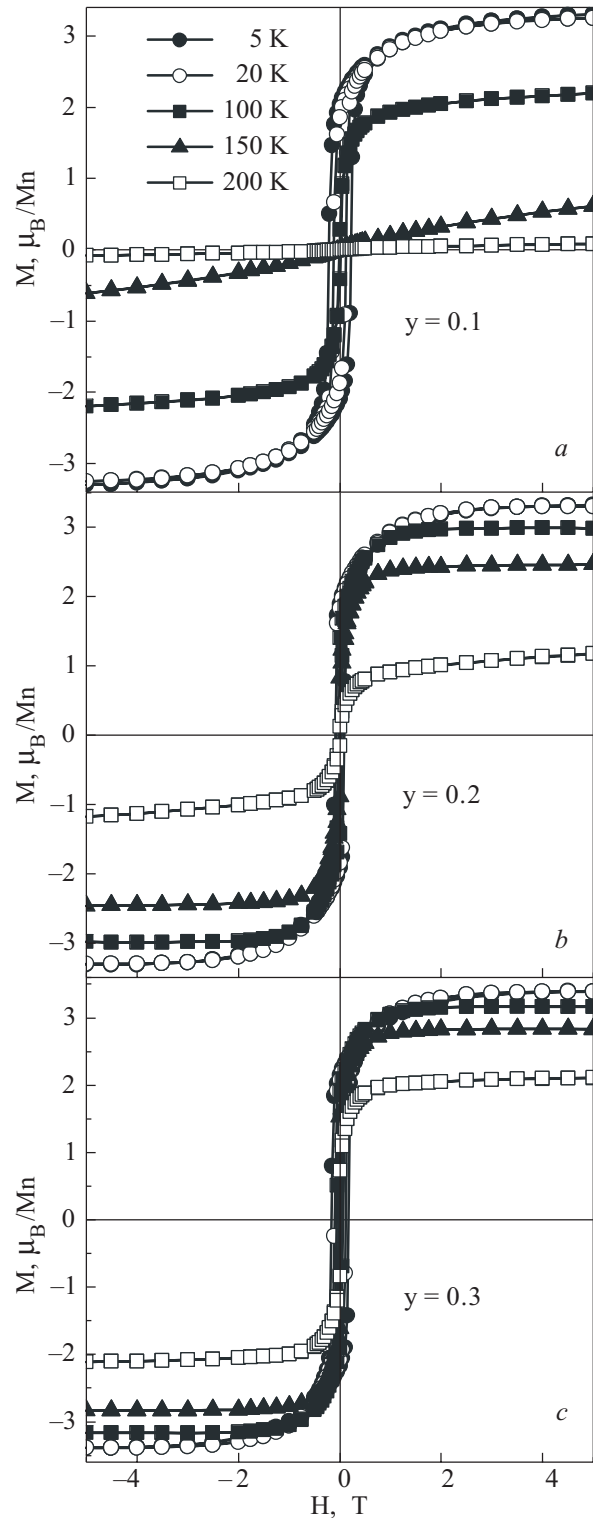

Fig. 4. Temperature dependences of the in-plane FC (solid symbols) and ZFC (open symbols) magnetic moment for the La$_{1-y}$Ce$_y$MnO$_3$ films with $y = 0.1$ (*a*), 0.2 (*b*) and 0.3 (*c*), measured at different applied magnetic fields. Lines are guides to the eyes.

Fig. 5. Magnetic-field dependences of the in-plane magnetic moment for the La$_{1-y}$Ce$_y$MnO$_3$ films with $y = 0.1$ (*a*), 0.2 (*b*) and 0.3 (*c*), measured at different temperatures. Lines are guides to the eyes.

crostructure perfection, which is higher for the LCMO8 film.

Figure 5 presents the in-plane hysteresis loops, $M(H)$, for the LCMO9 (*a*), LCMO8 (*b*) and LCMO7 (*c*) films taken at different temperatures. All films have almost the similar value of the saturation magnetic moment at 5 K, near 3.3 μ_B/Mn, which is higher than that was observed for the post-annealed films [24] while quite smaller of predicted by the theory [30]. It is seen more clearly on the temperature dependences of the saturation magnetic moment, $M_s(T)$, represented by Fig. 6,*a*.

Figure 6,*b* displays the in-plane hysteresis loops at 5 K for the films more in detail, which were measured in the ZFC (open symbols) and the FC (solid symbols) regimes. In last case the films were cooled down in the external magnetic field of 0.5 T. This experiment was car-
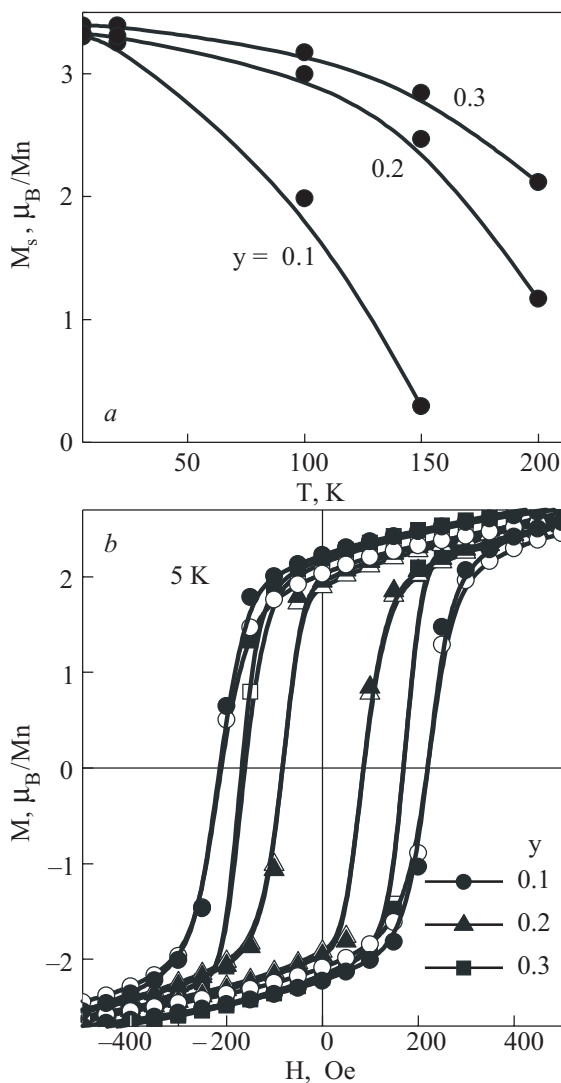
ried out for the feature testing of the exchange-bias-interaction effect, which has been observed in the hole-doped La$_{0.7}$Ca$_{0.3}$MnO$_3$ compound [31,32]. The main obvious indication of the existence of exchange bias is the shift of the hysteresis loop along the field axis after field cooling of the sample. However, in our case the hysteresis loops are symmetrical regardless of the cooling regime with a coercive field of $H_c \simeq \pm 216$, 83 and 167 Oe at $T = 5$ K for LCMO9, LCMO8 and LCMO7, respectively. Moreover, all films have almost the same remanent magnetic moment, $M_r \simeq 2.0\,\mu_B$/Mn, at this temperature. The observed minimal H_c value for LCMO8 can be is explained by the more perfect microstructure which is realized in this film, as was mentioned above.

Figures 7 shows the temperature dependence of resistance, $R(T)$, for the LCMO9 (*a*), LCMO8 (*b*) and

Fig. 6. (*a*) Temperature dependence of the in-plane saturation magnetic moment for the La$_{1-y}$Ce$_y$MnO$_3$ films. Lines are guides to the eyes. (*b*) The in-plane ZFC (open symbols) and FC (solid symbols) hysteresis loops for the same films measured at 5 K. The films were cooled down at $H = 0.5$ T.
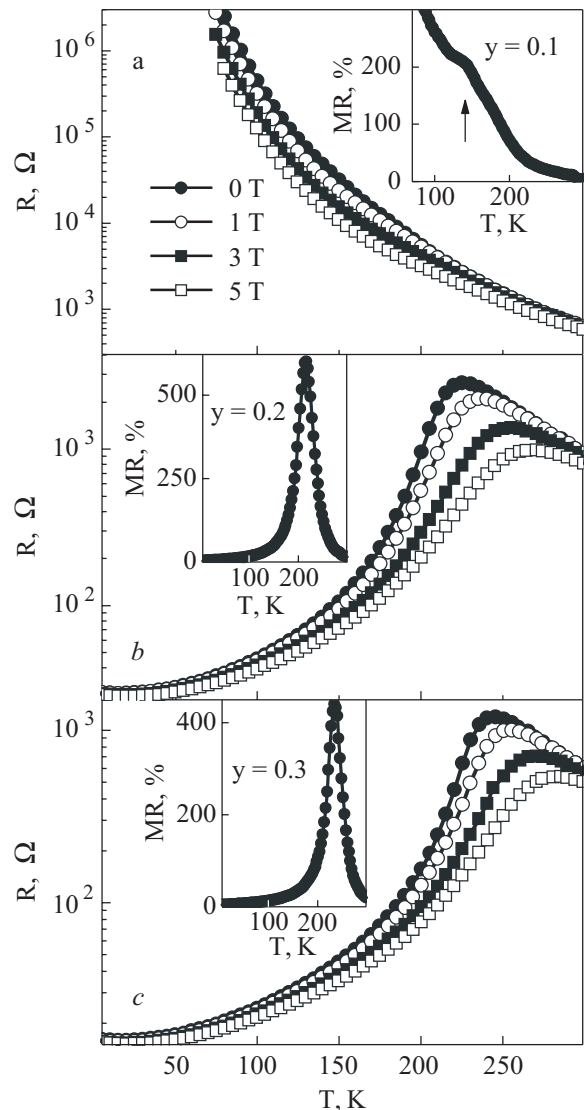
Fig. 7. Temperature dependence of resistance for the La$_{1-y}$Ce$_y$MnO$_3$ films with $y = 0.1$ (*a*), 0.2 (*b*) and 0.3 (*c*), measured at different applied magnetic fields. Lines are guides to the eyes. Insets show the corresponding temperature dependences of the magnetoresistance, MR (%).

Table 2. Magnetotransport characteristics for the investigated films

Samples	Curie point, T_C, K	Coercive field, H_c, Oe	Remanence, M_r / M_S, %	Magnetoresistance, MR, % [a]	MI transition, T_P, K	Activation energy, E_A, K
LCMO9	150	216	63	200	—	1700
LCMO8	250	83	58	600	225	1600
LSMO7	280	167	64	440	245	1400

[a] Maximal value at T_P, for LCMO9 at T_C.

LCMO7 (*c*) films measured at different applied magnetic fields. The magnetic field was directed parallel to the film surface and at right angle to the transport current. The insets presents the temperature-dependent magnetoresistance ratio, MR, for the corresponding films. Here the MR value is defined by $100\% \times [R(0) - R(H)]/R(H)$, where $R(0)$ and $R(H)$ are the resistances without and with a magnetic field of 5 T, respectively. It is seen that LCMO9 does not undergo the sharp transition in the metal state with decreasing temperature in the whole temperature interval while demonstrates the significant increase of MR(T) with the slight kink-like peculiarity near the Curie point, $T_C \simeq 150$ K (indicated by arrow). In contrast to that LCMO8 and LCMO7 manifest a typical for CMR $R(T)$ behavior with the well-defined metal–insulator (MI) transition at $T_P \simeq 225$ and 245 K and MR $\simeq 600$ and 440%, respectively.

The main physical parameters of the films are summarized in Table 2.

5. Discussion

The magnetic and transport properties of the investigated La$_{1-y}$Ce$_y$MnO$_3$ films are very similar to that for La$_{1-y}$Ca$_y$MnO$_3$ system. The decrease in Ce or Ca doping up to $y = 0.1$ leads to suppression of ferromagnetic ordering, which is accompanied by a significant decreasing of T_C, and a disappearance of the MI transition at all temperatures. Figure 8,*a* presents the $M(T)$ dependence of the spontaneous magnetization (without an applied magnetic field) for LCMO9. It is seen that after the well-defined increase of magnetic moment, which is connected with the FM transition at $T_C \leq 150$ K, the $M(T)$ begin to drop with decreasing temperature at $T \leq 80$ K. The evidence of the low-temperature magnetic transition is confirmed by the non-monotonic temperature behavior of the MR(T), which is represented by Fig. 8,*b*. In addition to the kink-like peculiarity at T_C, the MR(T) curve demonstrates a sharp bend at $T \leq 80$ K, indicating that the magnetic state of film is changed with decreasing temperature. For the La/Ca system of the same composition this phenomenon is explained by existence of the second ferromagnetic → canted antiferromagnetic transition which supervenes FM at once [33,34]. This explanation can be

used for description of magnetic behavior in the electron-doped LCMO9 film, as well. The FFT pattern (see Fig. 2,*e*) for this film presents the small regions of double-period modulated phase with a wave vector $q = a^*/2$,
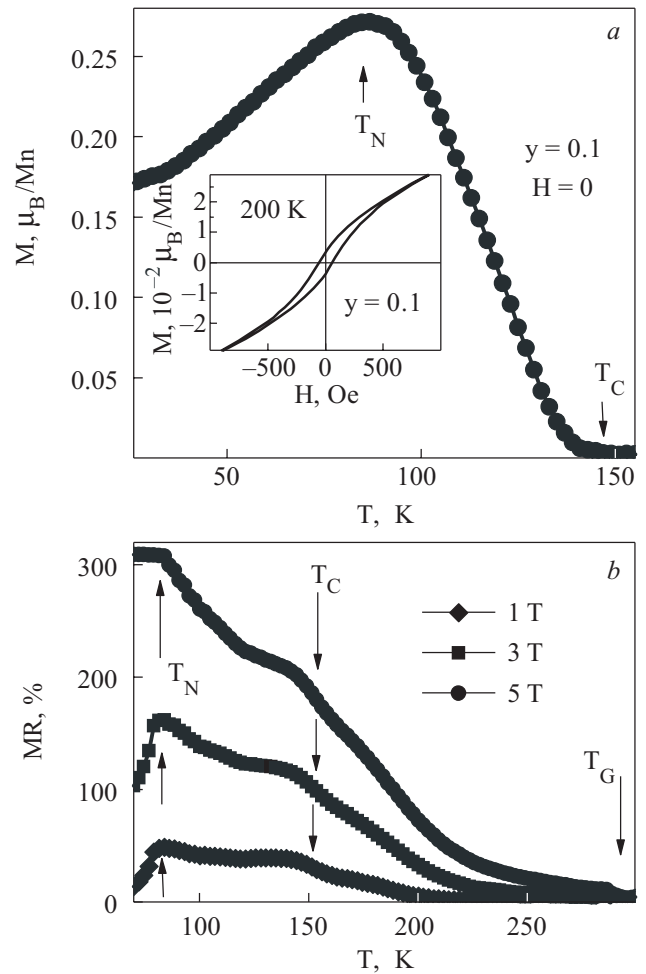

Fig. 8. (*a*) Temperature dependences of the spontaneous magnetization (without an applied magnetic field) for the La$_{0.9}$Ce$_{0.1}$MnO$_3$ film. Arrows indicate the FM (T_C) and the AFM (T_N) transition temperatures. Inset presents the $M(H)$ dependence for the same film taken at $T = 200$ K, which is significantly higher than Curie point. Lines are guides to the eyes. (*b*) Temperature dependences of magnetoresistance ratio at different applied magnetic fields. Arrows indicate the peculiarities on the MR(T) curves, connected with the corresponding magnetic transitions. T_G is the Griffiths temperature (see text).

which usually is treated as a formation of the charge-ordered antiferromagnetic (AFM) state (with the ordering of Mn^{2+} and Mn^{3+} ions). Consequently, the FM and the charge-ordered AFM phases are coexisted in the LCMO9 film at low temperatures ($T \leq 80$ K). However, in contrast to a well-known intrinsic phase-separation effect, which is very often observed in the hole-doped manganites and has an electronic origin [1], in our case these magnetic phases belong to the different crystal structures (modulated and unmodulated), which are controlled by the long-range Jahn–Teller interaction and arise due to a nonuniform distribution of the lattice strain during an epitaxial growth mode [21,22,35]. The HREM analysis reveals that the double-period modulated (AFM) phase, does not exceed a few percent of the film volume, and can not to have a serious influence on the total magnetic properties of the film. It is confirmed by the minor difference in the saturation magnetic moment at low temperature between films with a different Ce doping (see Fig. 6,*a*).

At the same time, another kind of the magnetic inhomogeneity is existent in LCMO9 film. Inset in Fig. 8,*a* presents the $M(H)$ dependence for LCMO9, taken at temperature, which is significantly higher than Curie point. The hysteretic behavior of the magnetization loop evidences the presence a few of the FM phase in the temperature range, where the film must be in the paramagnetic (PM) basic state. The chemical inhomogeneity of the film and the existence of long-term spin-ordered fluctuations (magnetic polaron clusters), can be main reasons for this phenomenon. It was shown recently that in $La_{0.9}Ce_{0.1}MnO_3$ film, deposited at the high oxygen pressure, Curie temperature reaches of 200 K [12]. The more reasonable explanation of this effect is based on the influence of the oxygen doping on the Mn^{3+}: Mn^{2+} ratio, which provides the magnetic ordering and the electron transport in these compounds. The ionic structure of this manganite according to Jonker and van Santen [36] is $La_{1-y}^{3+}Ce_y^{4+}Mn_{1-y+2\delta}^{3+}Mn_{y-2\delta}^{2+}O_{3-\delta}^{2-}V_\delta^O$, where V_δ^O stands for the ratio of oxygen vacancies. Consequently, the real Mn^{3+}: Mn^{2+} ratio is significantly dependent on the oxygen content. The oxygen deficiency leads to increase of the Mn^{3+}: Mn^{2+} ratio ($y \to 0$) while the overdoping by oxygen reveals the decreasing Mn^{3+}: Mn^{2+} ($y \to 1$). Therefore, the $La_{0.9}Ce_{0.1}MnO_3$ film, prepared at the high oxygen pressure [12], can not be treated as an exactly corresponding to the indicated stoichiometry, and the observed enhancement of FM ordering (increase of T_C) is governed by the increase in concentration of Mn^{2+}. On the other hand, the HREM analysis reveals the presents of regions with a strip-domain phase (see Fig. 3,*c*), which can be treated as a low-dimensional layered structure. The main peculiarity of such kind of structure is the existence of long-term spin-ordered fluctuations (magnetic polaron clusters) [37], which leads to the Griffiths

phase [38] formation above the FM transition point. In this case the magnetic moment can be written as $M(T,H) = M(0,H) \exp(-k_B T / \mu_{eff} H)$, where $M(0,H)$ is the magnetic moment at $T = 0$, k_B is the Boltzmann constant, and μ_{eff} is the effective magnetic moment of magnetic polaron cluster. Figure 9,*a* shows the $M(T)$ dependences for LCMO9 in the temperature range above Curie point at different applied magnetic fields. The solid lines are the corresponding theoretical curves, obtained within the framework of magnetic polaron model [37]. It is seen that the theoretical curves excellently agree with experimental ones up to about $T \simeq 300$ K, above which
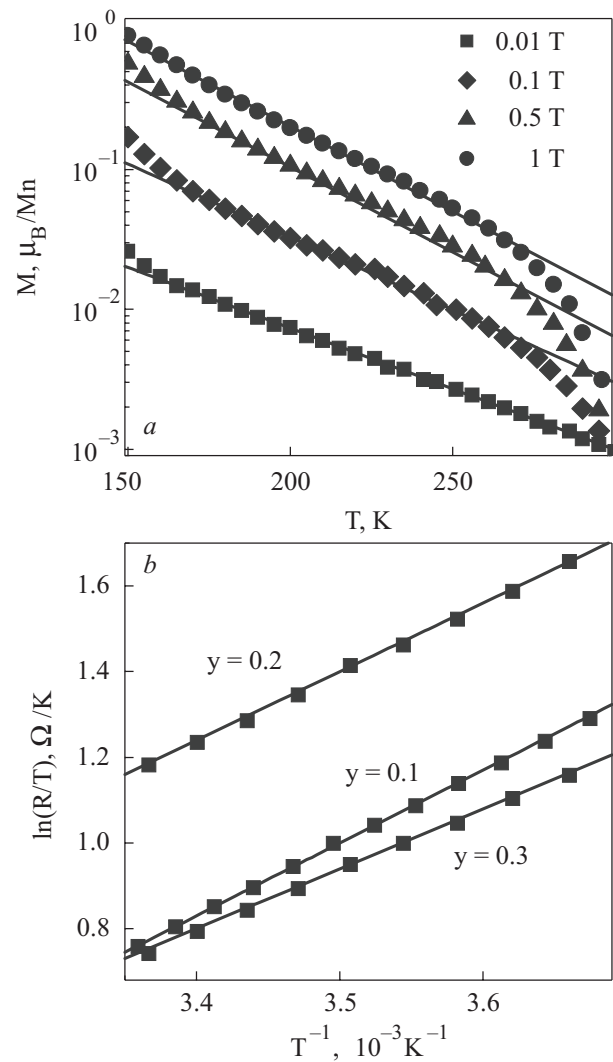

Fig. 9. (*a*) Temperature dependence of the in-plane FC magnetic moment for the LCMO9 film in the temperature range above Curie point at different applied magnetic fields. The solid lines are the corresponding theoretical curves, obtained within the framework of magnetic polaron model (see discussion in the text). (*b*) The ln (R/T) vs. T^{-1} plots for the $La_{1-y}Ce_yMnO_3$ films in temperature range above the corresponding Curie points. Solid lines are theoretical curves, obtained on basis of thermally-activated conductivity model (see discussion in the text).

the film transforms to the true PM state. Consequently, this temperature can be treated as the Griffiths one, $T_G \simeq 300$ K, and the temperature range between T_C and T_G is the area of existence of the Griffiths phase [39]. To avoid the PM contribution in magnetic moment, only the $M(T)$ curve, taken at lower magnetic field, is analyzed in detail. The following fitting parameters were obtained in this case: $M(0,H) \simeq 0.4\mu_B$/Mn site and $\mu_{eff} \simeq 7.5 \cdot 10^3 \mu_B$. By taking the saturation magnetic moment for the fully-FM state in this film as $3.3\mu_B$/Mn, the estimated average diameter of a magnetic polaron cluster in the Griffiths phase turns out to be 6.2 nm, which is very close to that for the La$_{0.4}$Ca$_{0.6}$MnO$_3$ film with inclusions of the similar strip-domain phase [22]. Figures 8,*b* manifests that the magnetoresistance effect for the LCMO9 film occurs at $T \leq T_G$, in other words in the Griffiths state, but without the MI transition below T_C with the decreasing temperature. First fact once more confirms the existence of long-term spin-ordered fluctuations at $T \geq T_C$ and the second one is explained by the deficiency of an itinerant electrons, which are necessary for formation of the conducting channel or the infinite cluster for theirs percolation [1].

Analysis of the HREM images for LCMO8 and LCMO7 (not shown) reveals that these films also have regions with the strip-domain phase and, as result, should be demonstrate the magnetic behavior typical for the Griffiths phase at $T \geq T_C$. However, since our setting was limited to room temperature, we could not carry out the $M(T)$ measurements in the temperature interval far higher of Curie points and realize the careful test of this assumption.

Figure 9 shows the $(\ln R/T)$ vs. T^{-1} plots in temperature range above the corresponding Curie points for the LCMO9, LCMO8 and LCMO7 films. These plots can be described on the basis of thermally-activated conductivity model which predicts an expression of $R(T) = R_0 T \exp(E_A/T)$ where E_A is the activation energy in unit of temperature. The best agreement between the experiment and the theory (solid lines) is seen with the activation energy values as $T_A \simeq 1700$, 1600 and 1400 K for LCMO9, LCMO8 and LCMO7, respectively. These values are very close to that for the La/Ca films and testify to the thermally-activated polaron mechanism of the conductivity in the PM state.

6. Conclusions

The electron-doped La$_{1-y}$Ce$_y$MnO$_3$ films ($y = 0.1$, 0.2 and 0.3) have been prepared by the pulse laser deposition on the LaAlO$_3$ (100) substrate. The microstructure analysis reveals that all films have a high *c*-oriented texture, the orthorhombic crystal lattice, excepting of $y = 0.1$, which manifests a slight rhombohedral distortion,

and the negligible quantity of CeO$_2$ inclusions. The observed strip-domain phase with a periodic spacing of about 3c, the crystal lattice of which is the same to the basic film phase, reveals the magnetic behavior typical for the Griffiths phase. The regions of the double-period modulated phase was found at room temperature in the $y = 0.1$ film, which are treated as the Mn^{3+}/Mn^{2+} ordering with the partial FM $\rightarrow$ AFM transition at $T_N \leq 80$ K. At the same time, the carried out investigation manifests that the magnetic and transport properties of the electron-doped La$_{1-y}$Ce$_y$MnO$_3$ films, driven by a cation doping, are similar to that for the hole-doped La/Ca manganites. Therefore, one can conclude, that does not exist of principle difference between the mechanisms of spin-ordering and charge-transport in the hole- and the electron-doped manganites.

1. For a review, see: *Colossal Magnetoresistance, Charge Ordering and Related Properties of Manganese Oxides*, C.N.R. Rao and B. Raveau (eds.), World Scientific, Singapore (1998); *Colossal Magnetoresistance Oxides*, Y. Tokura (ed.), Gordon and Breach, London (1999); E. Dagotto, T. Hotta, and A. Moreo, *Phys. Rep.* **344**, 1 (2001).
2. C. Zener, *Phys. Rev.* **82**, 403 (1951).
3. P.W. Anderson and H. Hasegawa, *Phys. Rev.* **100**, 675 (1955).
4. P.G. de Gennes, *Phys. Rev.* **118**, 141 (1960).
5. A.J. Millis, P.B. Littlewood, and B.I. Shraiman, *Phys. Rev. Lett.* **74**, 5144 (1995).
6. P. Mandal and S. Das, *Phys. Rev.* **B56**, 15073 (1997).
7. R. Ganguly, I.K. Gopalakrishnan, and J.V. Yakhmi, *J. Phys.: Condens. Matter* **12**, L719 (2000).
8. P. Raychaudhuri, S. Mukherjee, A.K. Nigam, J. John, U.D. Vaisnav, R. Pinto, and P. Mandal, *J. Appl. Phys.* **86**, 5718 (1999).
9. C. Mitra, P. Raychaudhuri, J. John, S.K. Dhar, A.K. Nigam, and R. Pinto, *J. Appl. Phys.* **89**, 524 (2001).
10. P. Raychaudhuri, C. Mitra, P.D.A. Mann, and S. Wirth, *J. Appl. Phys.* **93**, 8328 (2003).
11. W.J. Chang, C.C. Hsieh, J.Y. Juang, K.H. Wu, T.M. Uen, Y.S. Gou, C.H. Hsu, and J.Y. Lin, *J. Appl. Phys.* **96**, 4357 (2004).
12. T. Yanagida, T. Kanki, B. Vilquin, H. Tanaka, and T. Kawai, *J. Appl. Phys.* **97**, 033905 (2005).
13. D.J. Wang, J.R. Sun, S.Y. Zhang, G.J. Liu, B.G. Shen, H.F. Tian, and J.Q. Li, *Phys. Rev.* **B73**, 144403 (2006).
14. V.G. Prokhorov, G.G. Kaminsky, V.S. Flis, Y.P. Lee, K.W. Kim, and I.I. Kravchenko, *Physica* **B307**, 239 (2001).
15. A.G. Zaitsev, G. Ockenfuss, D. Guggi, R. Wördenweber, and U. Krüger, *J. Appl. Phys.* **81**, 3069 (1997).

16. A.Varez, E. Garcia-Gonzalez, and J. Sanz, *J. Mater. Chem.* **16**, 4249 (2006).

17. R. Mahendiran, S.K. Tiwary, A.K. Raychaudhuri, T.V. Ramakrishnan, R. Mahesh, N. Rangavittal, and C.N.R. Rao, *Phys. Rev.* **B53**, 3348 (1996).

18. O.I. Lebedev, G. Van Tendeloo, S. Amelinckx, H.L. Ju, and K.M. Krishnan, *Philos. Mag.* **A80**, 673 (2000).

19. G. Van Tendeloo, O.I. Lebedev, and S. Amelinckx, *J. Magn. Magn. Mater.* **211**, 73 (2000).

20. Y.P. Lee, S.Y. Park, Y.H. Hyun, J.B. Kim, V.G. Prokhorov, V.A. Komashko, and V.L. Svetchnikov, *Phys. Rev.* **B73**, 224413 (2006).

21. S.Y. Park, Y.H. Hyun, Y.P. Lee, V.L. Svetchnikov, K.W. Kim, and V.G. Prokhorov, *Appl. Phys. Lett.* **89**, 052502 (2006).

22. Y.H. Hyun, J.S. Park, T.W. Eom, G.H. Kim, Y.S. Lee, Y.P. Lee, V.G. Prokhorov, and V.L. Svetchnikov, *Appl. Phys. Lett.* **93**, 042515 (2008).

23. V.G. Prokhorov, G.G. Kaminsky, Y.P. Lee, S.Y. Park, Y.H. Hyun, J.S. Park, and V.L. Svetchnikov, *Fiz. Nizk. Temp.* **34**, 942 (2008) [*Low Temp. Phys.* **34**, 746 (2008)].

24. T. Yanagida, T. Kanki, B. Vilquin, H. Tanaka, and T. Kawai, *Phys. Rev.* **B70**, 184437 (2004).

25. F.L. Tang and X. Zhang, *Phys. Rev.* **B73**, 144401 (2006).

26. A.H. Chen, S.-W. Cheong, and H.Y. Hwang, *J. Appl. Phys.* **81**, 4326 (1997).

27. S. Mori, C.H. Chen, and S.-W. Cheong, *Nature (London)* **392**, 473 (1998).

28. M.T. Fernández-Díaz, J.L. Martínez, J.M. Alonso, and E. Herrero, *Phys. Rev.* **B59**, 1277 (1999).

29. P.G. Radaelli, D.E. Cox, L. Capogna, S.-W. Cheong, and M. Marezio, *Phys. Rev.* **B59**, 14440 (1999).

30. Q. Zhang and W. Zhang, *Phys. Rev.* **B68**, 134449 (2003).

31. M. Muroi, P.G. McCormick, and R. Street, *Rev. Adv. Mater. Sci.* **5**, 76 (2003).

32. J. Nogués, J. Sort, V. Langlais, V. Skumryev, S. Suriñach, J.S. Muñoz, and M.D. Baró, *Phys. Rep.* **422**, 65 (2005).

33. G. Biotteau, M. Hennion, F. Moussa, J. Rodriguez-Carvajal, L. Pinsard, and A. Revcolevschi, *Physica* **B259–261**, 826 (1999).

34. V.G. Prokhorov, V.A. Komashko, V.L. Svetchnikov, Y.P. Lee, and J.S. Park, *Phys. Rev.* **B69**, 014403 (2004).

35. M.J. Calderon, A.J. Millis, and K.H. Ahn, *Phys. Rev.* **B68**, 100401 (2003).

36. G.H. Jonker and J.H. van Santen, *Physica* **19**, 120 (1953).

37. V.M. Galitski, A. Kaminski, and S.D. Sarma, *Phys. Rev. Lett.* **92**, 177203 (2004).

38. R.B. Griffiths, *Phys. Rev. Lett.* **23**, 17 (1969).

39. Since the first works of Salamon et al. [40], the many evidences for Griffiths phase were found in the doped manganites [41–44]. However, a physical nature of its origin continues to remain very far from the complete understanding.

40. M.B. Salamon, P. Lin, and S.H. Chun, *Phys. Rev. Lett.* **88**, 197203 (2002); M.B. Salamon and S.H. Chun, *Phys. Rev.* **B68**, 014411 (2003); P.K. Chan, N. Goldenfeld, and M.B. Salamon, *Phys. Rev. Lett.* **97**, 137201 (2006).

41. J. Deisenhofer, D. Braak, H.-A. Krug von Nidda, J. Hemberger, R.M. Eremina, V.A. Ivanshin, A.M. Balbashov, G. Jug, A. Loidl, T. Kimura, and Y. Tokura, *Phys. Rev. Lett.* **95**, 257202 (2005).

42. W. Jiang, X.Z. Zhou, G. Williams, Y. Mukovskii, and K. Glazyrin, *Phys. Rev.* **B76**, 092404 (2007).

43. W. Jiang, X.Z. Zhou, G. Williams, Y. Mukovskii, and K. Glazyrin, *Phys. Rev.* **B77**, 064424 (2008).

44. P. Tong, B. Kim, D. Kwon, T. Qian, S.I. Lee, S.-W. Cheong, and B.G. Kim, *Phys. Rev.* **B77**, 184432 (2008).